SOFT ROBOTS

Multifunctional metallic backbones for origami robotics with strain sensing and wireless communication capabilities

Haitao Yang[1]*, Bok Seng Yeow[2]*, Zhipeng Li[3]*, Kerui Li[1], Ting-Hsiang Chang[1], Lin Jing[1], Yang Li[1], John S. Ho[3], Hongliang Ren[2], Po-Yen Chen[1,4]†

The tight integration of actuation, sensing, and communication capabilities into origami robots enables the development of new-generation functional robots. However, this task is challenging because the conventional materials (e.g., papers and plastics) for building origami robots lack design opportunities for incorporating add-on functionalities. Installing external electronics requires high system integration and inevitably increases the robotic weight. Here, a graphene oxide (GO)–enabled templating synthesis was developed to produce reconfigurable, compliant, multifunctional metallic backbones for the fabrication of origami robots with built-in strain sensing and wireless communication capabilities. The GO-enabled templating synthesis realized the production of complex noble metal origamis (such as Pt) with high structural replication of their paper templates. The reproduced Pt origami structures were further stabilized with thin elastomer, and the Pt-elastomer origamis were reconfigurable and served as the multifunctional backbones for building origami robots. Compared with traditional paper and plastic materials, the reconfigurable Pt backbones were more deformable, fire retardant, and power efficient. In addition, the robots with conductive Pt-elastomer backbones (Pt robots) demonstrated distinct capabilities—such as on-demand resistive heating, strain sensing, and built-in antennas—without the need for external electronics. The multifunctionality of Pt robots was further demonstrated to extend beyond the capabilities of traditional paper-based robots, such as melting an ice cube to escape, monitoring/recording robotic motions in real time, and wireless communications between robots. The development of multifunctional metallic backbones that couple actuation, sensing, and communication enriches the material library for the fabrication of soft robotics toward high functional integration.

INTRODUCTION

Origami denotes the ancient Japanese art of paper folding, where "ori" indicates folding and "kami" means thin papers. Origami structures are created from a sequence of programmable creases, providing a simple approach to reversibly transforming an object's shape, size, and motion (*1*, *2*). The rules of folding/unfolding are at the heart of many natural phenomena, and origami structures have been widely applied to drug delivery (*3*, *4*), aerospace communications (*5*, *6*), and deformable electronics (*7*, *8*). By exploiting high-DOF origami structures along with various actuation methods, reconfigurable origami robots have been created with unique attributes, including artificial muscles (*9*), self-folding machines (*10*), spring origami systems (*11*), and robotic metamorphosis (*12*). Conventional backbone materials for the fabrication of origami robotics include cellulose paper, polyester, polyether ether ketone, and polytetrafluoroethylene. The paper- and plastic-based backbones provide high mechanical stability for the fabricated origami robots, enabling them to undergo dynamic morphological changes and quick reconfiguration (*2*, *13*). Besides the mechanical support, the paper- or plastic-based backbones lack design opportunities for integrating additional capabilities into origami robots, such as stimuli responsiveness, tactile sensing, and wireless communication. Conventional strategies to incorporating add-on functionalities to origami robots involve engineering robotic backbones with functional materials or equipping new modules and external electronics (*14*–*17*). However, the equipment of additional modules often requires further system integration, and both strategies inevitably increase the overall weight of integrated origami robots, which contradicts the ultimate goals of creating light, compliant, power-efficient, and eventually untethered robots with multifunctionality (*2*). Therefore, instead of installing external devices, it is desirable to develop multifunctional soft backbones for origami robots to achieve tight integration of desired robotic functions, such as dynamic shape changes, strain sensing, and wireless communication between units (*18*, *19*).

Electrically conductive materials and their composites—such as thin metallic sheets (*20*), amorphous carbon (*21*), and two-dimensional (2D) materials (*22*)—have been demonstrated as new backbone materials to fabricate complex origami structures. Compared with paper- or plastic-based origami, electrically conductive origami structures are expected to facilitate the development of multifunctional origami robots with sensing and communication capabilities. However, most of the reported conductive origami structures were composed of rigid folding patterns, which were not deformable or stretchable, limiting their applications from mechanically dynamic actuators and robots (*20*–*22*). To the best of our knowledge, prototypical soft robots including conductive origami backbones with desired sensing and communication capabilities have not been demonstrated. Therefore, a new fabrication scheme is required to produce mechanically stable, soft, and conductive robotic backbones. The unconventional material library allowed us to exploit multifunctional backbones as built-in sensors and antennas, and the fabricated origami robots could couple sensing and communication capabilities without incorporating external electronics.

[1]Department of Chemical and Biomolecular Engineering, National University of Singapore, Singapore 117585, Singapore. [2]Department of Biomedical Engineering, National University of Singapore, Singapore 117583, Singapore. [3]Department of Electrical and Computer Engineering, National University of Singapore, Singapore 117583, Singapore. [4]Department of Chemical and Biomolecular Engineering, University of Maryland, College Park, MD 20742, USA.
*These authors contributed equally to this work.
†Corresponding author. Email: checp@nus.edu.sg

One potential route for the creation of multifunctional robotic backbones is to conduct the templated synthesis within the confined spacing of 2D material multilayers. The graphene oxide (GO) multilayer was used for the intercalation of various metal ion precursors, followed by high-temperature annealing/calcination processes. This intercalation templating synthesis enabled the reproduction of many higher-dimensional GO structures into a variety of metal oxide replicas, such as microtextures (*23*), freestanding strands (*24*), and complex origami structures (*25*). With excellent chemistry control and structural replication, we expect that the GO-derived synthesis exhibits high potential in producing complex metallic architectures, which can be further stabilized and used as the multifunctional backbones for soft robots.

RESULTS

Figure 1A illustrates the GO-enabled templating synthesis to convert cellulose paper films/origamis into various metal replicas with high structural preservation. The synthesis processes involved four steps. First, a phoenix-shaped cellulose template was immersed into GO dispersion, and the GO nanosheets were conformally coated onto the cellulose fibers after being air-dried [scanning electron microscope (SEM) image in Fig. 1A (i and ii)]. The deposition of GO nanocoating was about 15 weight % (wt %) of the cellulose template. The composite of GO-coated cellulose paper (abbreviated as GO-cellulose) was used as a sacrificial template for the growth of various noble metals (Fig. 1A, ii). The GO-cellulose template was then soaked in the precursor solution containing noble metal salts (M^{n+}) for 12 hours (e.g., $AuCl_3$, $AgNO_3$, and $PtCl_4$ with a concentration of 0.1 M; see more details in Materials and Methods). The negative charges on the surfaces of GO nanosheets ($\zeta \sim -45$ mV) along with the concentration gradients offered substantial driving force to recruit M^{n+} from bulk solution to the GO-cellulose templates (*26*). The hydrated GO nanocoatings exhibited expanded interlayer spacings (>12 Å), so the ions were unimpededly intercalated into the stacked GO films [x-ray diffraction (XRD) spectra in fig. S1A] (*27*). The intercalated metal ions were coordinated with one or multiple carboxylate group(s) on the GO nanosheets [m–$RCOO^- + M^{n+} \leftrightarrow -(RCOO)_mM^{(n-m)+}$] (*28*), resulting in a M^{n+}-intercalated GO-cellulose complex (abbreviated as M-GO-cellulose).

The M-GO-cellulose complexes then underwent two-stage annealing/calcination processes at 800°C in argon and at 500°C in air.

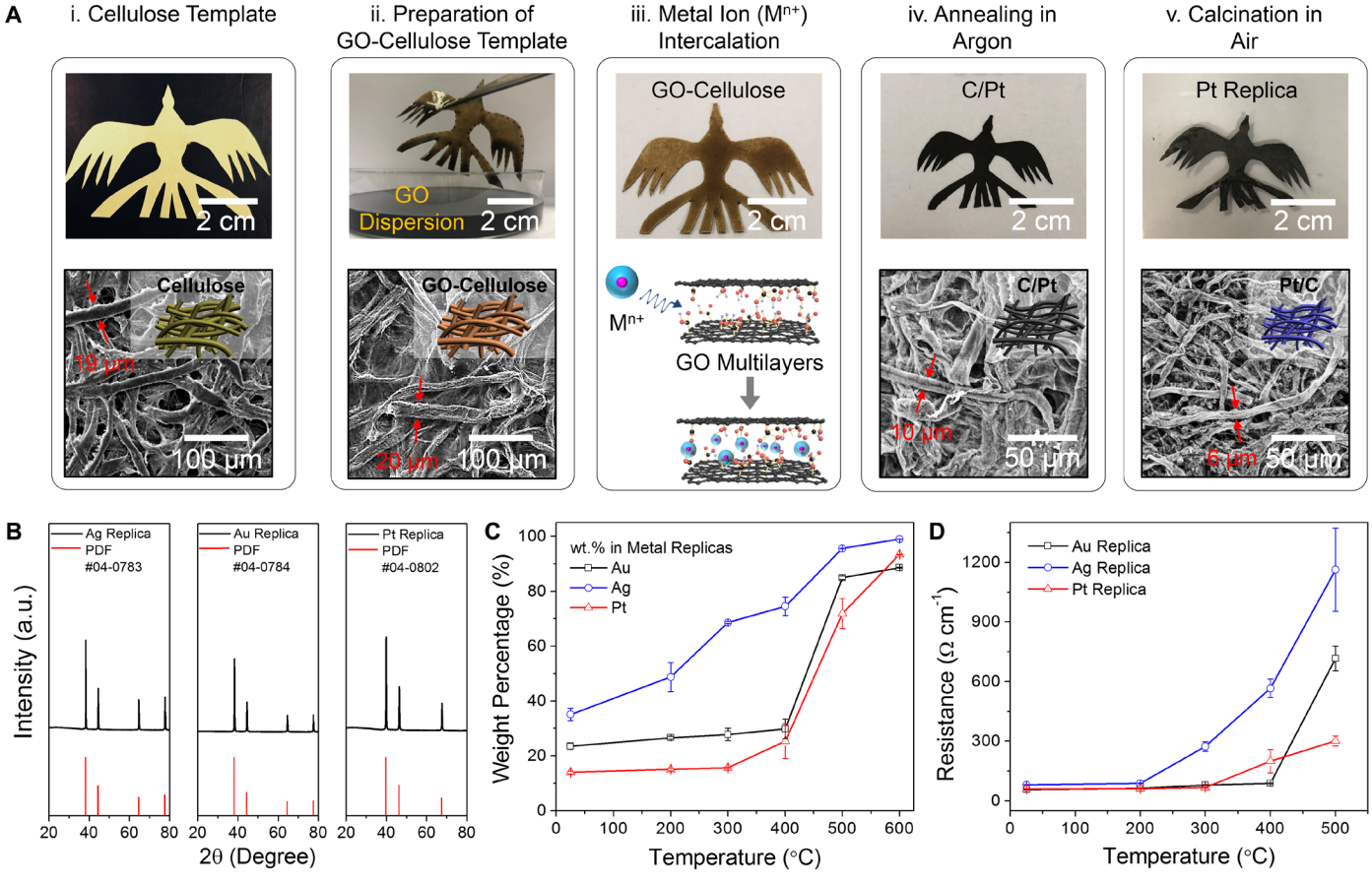

Fig. 1. GO-enabled templating synthesis of noble metal replicas. (**A**) The GO-enabled templating synthesis for transforming cellulose paper to noble metal replicas. The synthesis of a phoenix-shaped Pt replica is demonstrated. The SEM images showed that the network morphologies of cellulose paper and GO-cellulose template were very similar. The diameter of microfibers decreased from ~20 to ~6 μm after two-stage annealing/calcination. (**B**) XRD spectra of as-synthesized metal replicas after two-stage annealing/calcination. The spectra were consistent with their corresponding "powder diffraction files (PDF)" from "joint committee on powder diffraction standards." (**C**) Weight percentages of metallic contents in the templated replicas after the calcination in air at different temperatures. The weight percentages are determined by EDS analysis. (**D**) Resistance of templated metal replicas (across 1 cm) after the calcination in air at different temperatures. The error bars indicate the differences in measurements from four samples.

During the first-stage annealing in argon, the cellulose template was first carbonized into carbon, and the GO nanocoating was thermally reduced into reduced GO (rGO) (XRD patterns in fig. S1B). The bound metal ions were liberated and reduced back to noble metal nanocrystals in the rGO multilayers (*29*–*31*), producing C/Ag, C/Au, and C/Pt replicas with the mass losses of 90, 83, and 79 wt %, respectively. The digital and SEM images of phoenix-shaped C/metal intermediate products are shown in Fig. 1A (iv) and fig. S2. Afterward, the C/metal intermediate products underwent next-stage calcination in air to burn off the carbon for the synthesis of metal replicas. The XRD patterns in Fig. 1B demonstrate successful synthesis of Ag, Au, and Pt replicas after the two-stage annealing/calcination. As shown in Fig. 1A (v) and fig. S2, the metal replicas reproduced both the macroscale phoenix shape and the microporous network of GO-cellulose template well.

The composition of metal replicas was able to be controlled by tuning the calcination temperature in air. We produced multiple metal replicas under different calcination temperatures, and the compositions of metal replicas were quantitatively characterized by energy-dispersive x-ray spectroscopy (EDS) analysis (figs. S3 to S5). The weight percentages of Au and Pt started to increase as the calcination temperature increased over 400°C (Fig. 1C). The lower-temperature carbon oxidation in C/Ag products was due to the high loading of Ag nanocrystals (~35 wt %), which served as catalysts to enhance the oxidation rate, consistent with the previous reports (*32*). As the calcination temperature increased to 500°C, more amorphous carbon was oxidized (Raman spectra and related discussion in fig. S6), and the weight percentages of Ag, Au, and Pt nanocrystals reached to 95.5, 84.9, and 71.9 wt %, respectively, where the carbon component mainly came from the unoxidized rGO.

After the calcination at 500°C, the resistances of Au, Ag, and Pt replicas increased from 80 to 720 ohms, from 50 to 1,160 ohms, and from 60 to 300 ohms (across 1 cm), respectively (Fig. 1D). The increased resistance was due to less carbon in the noble metal replicas under high calcination temperature. The carbon provided additional electrical pathways to interconnect the templated noble metal microfibers and thus increased the electrical conductivity of metallic backbones. More details regarding the synthesis of metal replicas can be found in figs. S7 and S8, and more discussion is provided regarding the effect of carbon on the dimension shrinkage and mechanical flexibility of noble metal replicas in the Supplementary Materials. To produce the metal replicas with high structural replication, optimal metal loadings, and large mechanical flexibility, we set the calcination temperature at 500°C in the following studies and robotic fabrication. As shown in the SEM images in Fig. 1A and fig. S2, the C/metal intermediate products and metal replicas showed very similar fibrous network structures that were composed of the metallic microfibers with smaller diameters. We demonstrated that the GO nanosheets were necessary for the templating synthesis to achieve 3D origami replicas in noble metals. We first folded a planar paper into a wavy structure with four folds as the origami template. With the incorporation of GO nanosheets, we were able to produce a downsized wavy Pt replica with an unchanged number of folds (Fig. 2A, bottom). We carried out a similar templating experiment without

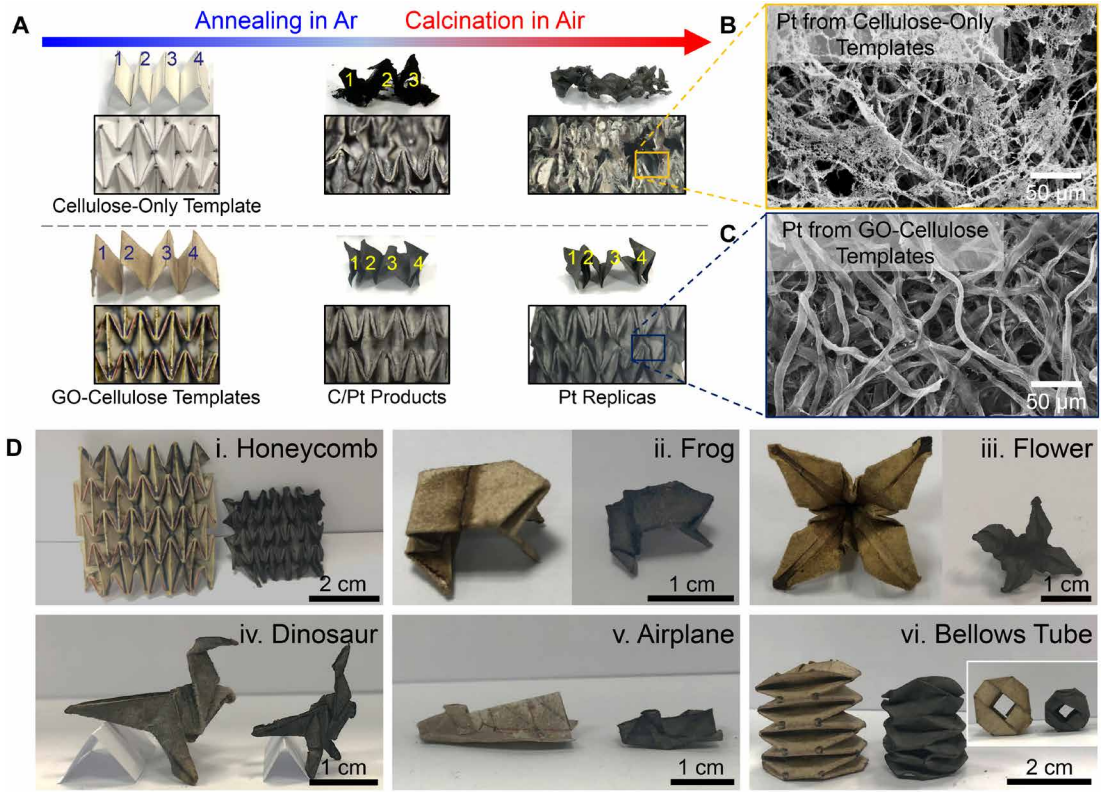

Fig. 2. Fabrication of metal origami structures. (**A**) Photos of the fourfold and auxetic hexagonal metal origami products synthesized from cellulose-only (top row) and GO-cellulose templates (bottom row). Pt-based products at different annealing/calcination stages are shown. SEM images of Pt products synthesized from (**B**) cellulose-only and (**C**) GO-cellulose templates. (**D**) Photos of GO-cellulose origami and as-templated downsized Pt origami replicas, including (i) honeycomb, (ii) frog, (iii) flower, (iv) dinosaur, (v) airplane, and (vi) bellows tube.

the deposition of GO nanocoatings in which the metal ions were directly absorbed into the wavy paper template, followed by the sequential annealing/calcination processes. The resulting Pt product did not resemble the original wavy structure (Fig. 2A, top).

The incorporation of GO nanosheets was required for the templated synthesis of complex origami structures (e.g., auxetic hexagonal honeycomb) (Fig. 2A), and the successful replication of origami structures was due to multiple reasons. First, the GO nanosheets exhibited rich functional groups to form the complexation with metal ions, and more precursors were involved for the construction of 3D metallic origami replicas. For instance, the weight of the Pt product synthesized from the cellulose-only template (without GO, 1.6 wt % of original paper template) was ~40% lower than the one from the GO-cellulose template (2.7 wt % of original paper template) (fig. S9). Second, the GO nanosheets served as the nanoscale templates to direct the growth of metal nanocrystals along the cellulose fibers. The presence of GO nanosheets can guide the growth of Pt nanocrystals along the 2D gallery spaces, enabling the successful replication of microfiber networks. As shown in Fig. 2B, the Pt structure from the cellulose-only template did not replicate the cellulose network well and exhibited higher porosity (49%, quantified by the measurements of grayscale line profiles of the micrographs and photos using ImageJ), and the Pt microfibers had smaller diameters (~3 μm) in comparison with those of the GO-enabled Pt structures (29% porosity, Pt microfibers with a 6-μm average diameter; Fig. 2C). From the EDS mapping in fig. S10, with the incorporation of GO nanosheets, the Pt nanocrystals were uniformly distributed across the produced metal replicas. The sintering of Pt nanoparticles (~6 nm) resulted in the formation of 2D interconnected particle arrays as the basic nanoscale building blocks [transmission electron microscope (TEM) images in fig. S11]. With the effective templating synthesis, we converted various 3D origami structures from cellulose paper into Pt, including honeycomb, frog, flower, dinosaur, airplane, and bellows (Fig. 2D). In comparison with their original paper templates, the spatially organized origami patterns were well preserved in the Pt replicas.

The mechanical stability of templated origami structures was further improved by the incorporation of thin elastomer, and the elastomer-stabilized metallic origami exhibited large deformability that enabled reversible reconfiguration. We focused on the Pt replicas due to efficient structural preservation, high mechanical flexibility, and high electrical conductivity, compared with the Au and Ag structures. After the templated Pt replicas were synthesized, dilute elastomer solution [uncured polydimethylsiloxane (PDMS) in dichloromethane; see Materials and Methods] was gradually infiltrated into the cellulose-templated Pt network (Fig. 3A). Followed by the curing process at 70°C, the Pt network was conformally coated with thin elastomer. The thickness of elastomer coating, the electrical conductivity, and the mechanical flexibility of the resulting Pt-elastomer backbones were controlled by the concentration of PDMS solution. As shown in figs. S12 and S13, when the PDMS concentration increased from 100 to 500 mg ml^{-1}, the thickness of Pt-PDMS backbones increased from 88 to 157 μm, the film resistance increased from 70 to 6400 ohms (across 1 cm), and the Young's moduli decreased from 14.2 to 5.7 MPa. Therefore, to ensure high electrical conductivity and sufficient mechanical flexibility for metallic backbones, we set the PDMS concentration at 300 mg ml^{-1}. The optimized Pt-elastomer backbone was obtained with the thickness of ~90 μm (SEM images in Fig. 3B), about 2.7 times thinner than the cellulose paper (thickness, ~250 μm). The Pt thin film with thin elastomer coating was more compliant (Young's modulus at ~10 MPa) than as-synthesized Pt film (320 MPa) and the original cellulose paper (580 MPa); the stress-strain curves are shown in fig. S13. The planar Pt-elastomer composite was able to sustain large and repeated deformations (180° bending, 360° twisting, and 30% stretchability) (Fig. 3C).

The Pt-elastomer origamis can be categorized as reconfigurable metamaterials and serve as a multifunctional backbone for the fabrication of soft robots. With the templated auxetic hexagonal patterns, the Pt-elastomer origamis were able to sustain repeated morphological changes under uniaxial strains. The strain-stress curves of Pt-elastomer origamis are shown in Fig. 3D, and the mechanical properties remained unchanged during the 200-cycle fatigue test. As shown in the in situ SEM images in Fig. 3E, whereas the Pt-elastomer origami was stretched, the replicated crease patterns were flattened to relieve the uniaxial strains. Figure 3F demonstrated that the auxetic hexagonal origami of Pt-elastomer was able to undergo the compressing/stretching processes to relieve the strains in both horizontal (x axis, −25 to 120%) and vertical directions (y axis, −5 to 20%).

Furthermore, the conductive Pt-elastomer origamis demonstrated intrinsic strain sensing capability and were used as built-in strain sensors, allowing the users to monitor the robotic actuations in real time without the integration of external sensors. The Pt replica was composed of interconnected conductive microfibers that well replicated the cellulose networks of paper template. As shown in SEM images inserted in Fig. 3G, when a planar Pt replica was gradually bent from 0° to 60°, the conductive microfibers in the high-curvature region became less interdigitated; the templated Pt network was further fractured under 90° bending. After the planar Pt replica was stabilized with elastomer, the electrical resistance of Pt-elastomer composite was responsive to bending, where the relative resistance changes increased linearly with the degree of bending (Fig. 3G). As a flat Pt-elastomer film was repeatedly flapped, the electrical resistance was fluctuated at the same frequency, enabling the recording of reversible bending behaviors (fig. S14).

Because the planer Pt-elastomer film was sensitive to the bending angles, we further investigated the strain sensing capability of Pt-elastomer origami backbones. The strain sensing performance of Pt-elastomer origami was evaluated by its gauge factor (GF), which was calculated using Eq. 1

$$\mathrm{GF} = \frac{(R_s - R_0)/R_0}{\varepsilon} \quad (1)$$

where ε denotes the in-plane strain and R_0 and R_s represent the initial resistance and the resistance under origami elongation (uniaxial stretching), respectively. The strain sensing performance in terms of GF is highly relevant to the number of origami folds along the stretching direction because the Pt microfibers on the creases became less interconnected under bending, leading to higher electrical resistance. The relative resistance changes of various Pt-elastomer origamis (including auxetic hexagonal honeycomb and bellows) were characterized under different uniaxial strains (Fig. 3H). With ~60 folds along the direction of stretching, the auxetic hexagonal Pt origami achieved a GF of 1.3 up to 60% strain. On the other hand, the Pt bellows tube (with 32 folds) was able to be stretched to 175% with a GF of 0.06.

The mechanically stable Pt-elastomer origamis were next demonstrated for the fabrication of origami robots/actuators with different actuation systems. For instance, we first produced a fully enclosed Pt tubular bellows replica (~37 volume % of the original paper template;

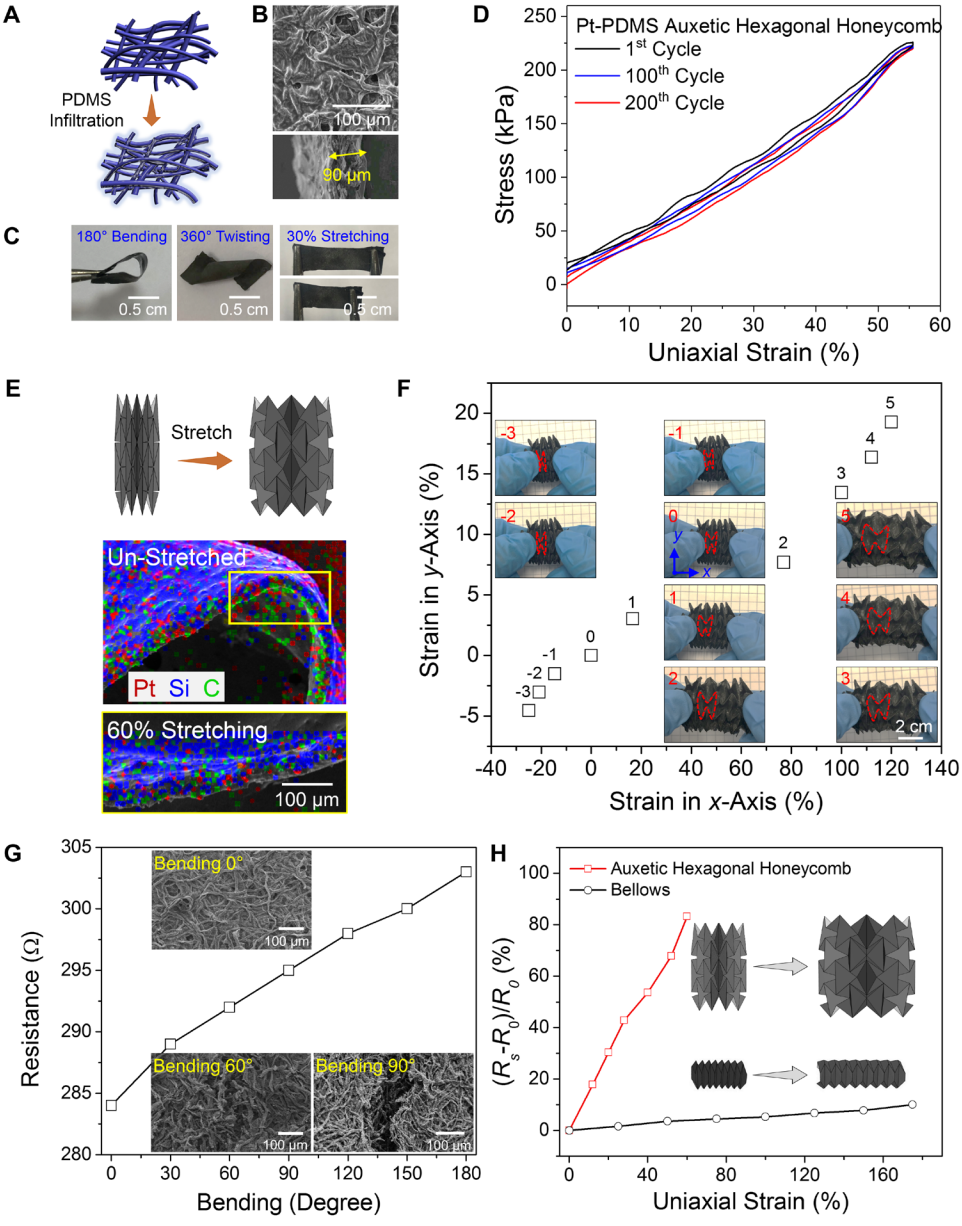

Fig. 3. Turning Pt origami replicas into deformable Pt-elastomer metamaterials. (**A**) Infiltration of dilute elastomer liquid into templated Pt replicas enables the fabrication of Pt-elastomer metamaterials. (**B**) Top-down and cross-sectional SEM images of Pt-elastomer composite. The thickness of Pt-elastomer composite is about 90 μm. (**C**) Large deformability of a planar Pt-elastomer thin film (180° bending, 360° twisting, and 30% stretching). (**D**) Stress-strain curves of a Pt-elastomer auxetic hexagonal origami during the stability test for 200 cycles. (**E**) In situ SEM images with EDS mapping of a Pt-elastomer crease under 90% uniaxial stretching. (**F**) The patterns of Pt-elastomer auxetic hexagonal origami is strain dependent during the uniaxial compressing (marked with −1 to −3) and stretching processes (marked with 1 to 5). The figure marked with 0 represented the initial state. (**G**) Resistance changes of a flat Pt-elastomer film under bending from 0° to 180°. (**H**) Relative resistance changes of auxetic hexagonal and bellows Pt-elastomer origamis under various uniaxial strains. R_s is the resistance of Pt-elastomer origami under uniaxial strains; R_0 is the resistance of unstrained Pt-elastomer origami.

fig. S15). The downsized Pt tube was further stabilized with thin elastomer coating and connected to an air pump for the fabrication of a pneumatic Pt origami robot (abbreviated as the single-bellows Pt robot). As the gas pressure increased, the bellows patterns of Pt robots were gradually unfolded, leading to the axial elongation of robotic body. As the gas pressure decreased, the robotic shape and length recovered accordingly. The directional friction of bellows-type Pt robots came from the "friction feet" installed at the head and tail (fig. S16). During repeated pneumatic actuations, the friction feet were able to reversibly move back and forth to generate enough friction force to push the bellows-type robots forward. This cyclic axial motion enabled the single-bellows Pt robot to crawl forward at a speed of 0.2 cm s^{-1}. The auxetic hexagonal origami in Pt-PDMS was also connected with shape-memory alloy (SMA) wires (i.e., nitinol) for the fabrication of an SMA-actuated Pt actuator (abbreviated as the auxetic hexagonal–type Pt actuator), which was able to be bent reversibly up to 60° (see detailed fabrication in Materials and Methods).

The reconfigurable metallic backbones introduced multiple distinct functionalities to origami robots. First, the metallic backbones were intrinsically fire retardant, allowing the fabricated Pt robots to sustain direct contact with the flame of an ethanol burner (flame temperature, ~800°C) for 30 s, whereas the paper robot was ignited within 5 s (Fig. 4A). Second, because the annealing/calcination processes removed most of the carbonaceous components (i.e., cellulose and GO), the Pt-elastomer backbone was about three times thinner (90 μm) and lighter (e.g., a Pt-elastomer bellows tube was 0.5 g) than the cellulose paper predecessor (thickness, ~250 μm; a paper bellows tube was 1.6 g). Third, the elastomer-stabilized metallic backbone (Young's modulus, ~10 MPa) was more compliant than the cellulose paper (Young's modulus, 580 MPa) yet did not sacrifice the mechanical stability for reversible robotic actuation. With the lightweight and mechanically complaint backbone, the Pt robot was more power efficient compared with the paper-based robot with the same dimensions (height, 2 cm; length, 3.5 cm). The number of origami folds and the thickness of backbone (~100 μm) were also controlled to be similar (figs. S17 and S18). The required pressure to pneumatically actuate the single-bellows paper and the Pt robots (at the same size) was recorded; the degree of elongation/contraction and the frequency of robotic actuations were controlled to be similar for a fair comparison. As shown in Fig. 4B and movie S1, the paper robot required larger pressure changes, from −3.9 to 11.9 kPa, for reversible elongation/contraction,

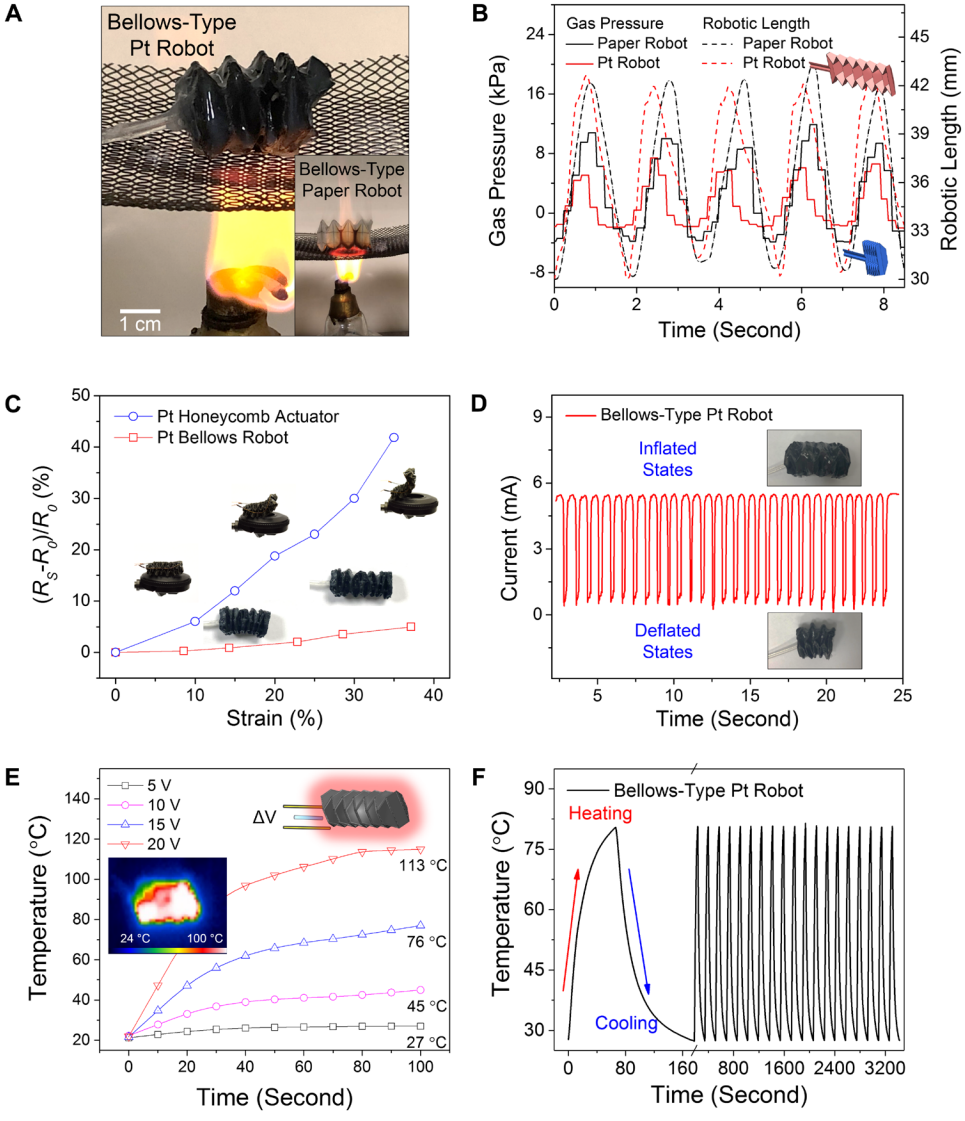

Fig. 4. Origami Pt robot with distinct capabilities. (**A**) Bellows-type Pt robot remained intact after 30-s fire test, whereas paper robot was ignited. (**B**) Robotic displacement and corresponding gas pressure of bellows-type Pt and paper robots. Both robots were fabricated with the same size (height, 2 cm; length, 3.5 cm). (**C**) Relative resistance changes of auxetic hexagonal–type Pt actuators (by nitinol wires) and bellows-type Pt robot (actuated by a pneumatic pump) under various strains. (**D**) Relative resistance changes of a bellows-type Pt robot during the actuation frequency at 1.2 Hz. (**E**) Surface temperature profiles of a bellows-type Pt robot as a function of time under 5, 10, 15, and 20 V. (**F**) Cycling test of resistive heating performance of a Pt robot under an applied voltage of 20 V.

yet lower pressure changes were needed for the Pt robot, from −3.7 to 7.4 kPa.

We further compare the crawling speed of three dual-bellows robots with other possible backbone materials, including cellulose paper, Pt-PDMS, and commercial aluminum foil (AF) (fig. S19, A and B). The fabrication of a dual-bellows Pt robot is schematically illustrated in fig. S20. The directional friction of bellows-type Pt robots came from the friction feet installed at the head and tail (fig. S21). During repeated pneumatic actuations, the frication feet were able to reversibly move back and forth to generate enough friction force to push the dual-bellows robots forward. The required gas pressure for three robots was recorded in fig. S19C, and the energy consumption of each robot was also calculated in fig. S19D (detailed calculation methods in Materials and Methods). The paper and Pt robots showed a similar crawling speed of ~0.5 cm s^{-1}, but the AF robot was slower (~0.3 cm s^{-1}). The AF and paper robots consumed 1170 and 510 J for an 8-cm displacement, respectively, whereas the Pt robot only consumed 336 J for the same crawling distance. The lower energy consumption of Pt robot resulted from its lighter and more compliant Pt-PDMS backbones (Young's modulus, ~10 MPa) in comparison with AF (~70 GPa) and cellulose papers (580 MPa).

As shown in Fig. 4C, both auxetic hexagonal–type Pt actuator and single-bellows Pt robot exhibited stable strain sensing performances with GFs of 1.2 and 0.17, respectively, which were similar to the performance of Pt-elastomer origamis and did not get disrupted after the robotic fabrication. The single-bellows Pt robot also demonstrated reliable durability during the stretching/relaxation cycles (1.2 Hz, up to 60% strain) (Fig. 4D). In addition, because of the electrically conductive backbone, the Pt origami robot was able to serve as a reconfigurable resistive heater for on-demand thermal management. When the bellows-type Pt robot was under an applied voltage of 20 V (detailed implemented setup was described in Materials and Methods), the Pt robot was quickly heated to above 100°C in 90 s (Fig. 4E), which was still capable of actuating reversibly and crawling forward. The Pt robot was able to be repetitively warmed up without degrading the heating performance or actuation capability (Fig. 4F).

In addition, the conductive Pt origami can send/receive electromagnetic (EM) waves and serve as a reconfigurable antenna to facilitate the development of origami robots with wireless communication capability. To explore the potential of using Pt robots as radiating antennas, we first conducted far-field calculation to obtain the simulated 3D radiation patterns of two Pt bellows tubes, which served as two halves of a dipole antenna (Fig. 5A). The simulated results exhibited an asymmetrical radiation pattern with strong electric fields in the *x* direction (the simulation method is described in Materials and Methods), indicating that the EM waves were preferably transmitted along the axis of bellows tubes. The fabrication of a dual-bellows Pt robot is schematically illustrated in Fig. 5B, and the Pt robot can be used as a reconfigurable dipole antenna. The dipole antenna with two Pt bellows tubes was fed by electrical signals via a SubMiniature version A connector with the coaxial cable. The SubMiniature connector was attached to the center of the plastic or paper cover, the connection between SubMiniature

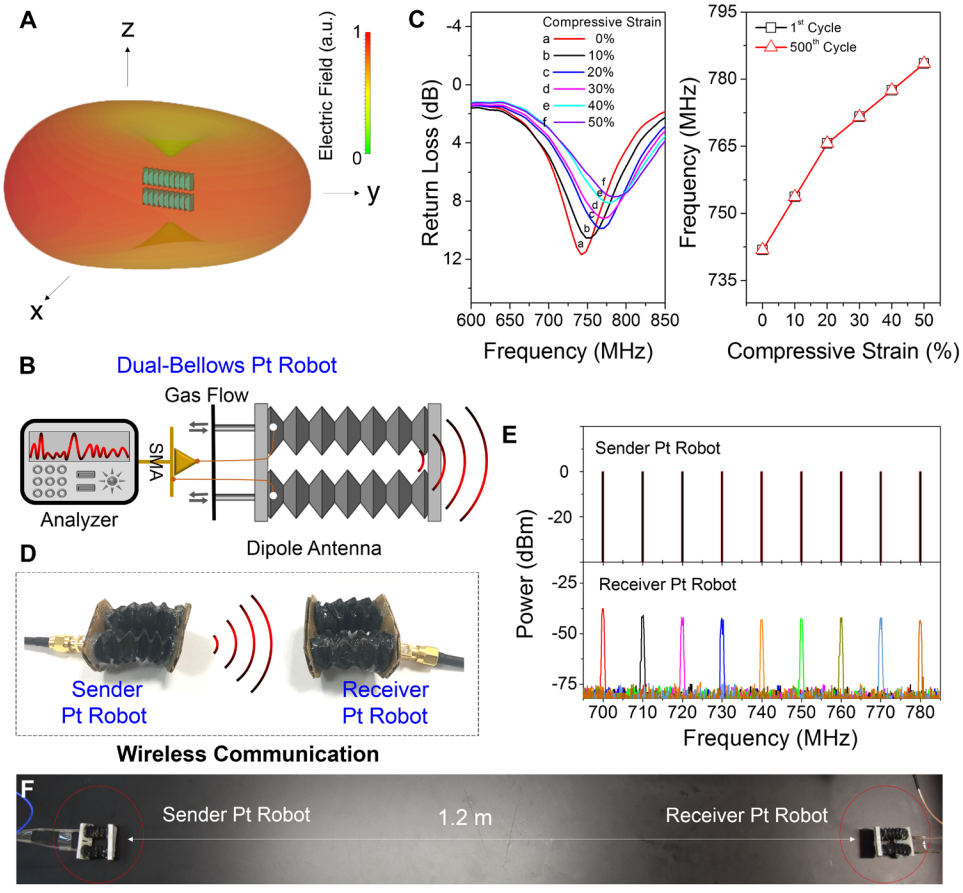

Fig. 5. Origami Pt robot with built-in wireless communication capabilities. (**A**) Simulated 3D radiation patterns for two Pt-elastomer bellows tubes at 741.8 MHz under 0% strain. (**B**) Schematic demonstration of a dual-bellows Pt robot, which also served as a reconfigurable dipole antenna. (**C**) Left: Return loss of the reconfigurable dipole antenna under different compressive strains from 0 to 50%. Right: The resonant frequencies are a function of compressive strains before and after 500-cycle robotic actuations. (**D**) Photograph of a sender Pt robot (sending signals) (left) and a receiver Pt robot (receiving signals) (right). (**E**) The pulse signals (the sender Pt robot sent) were well received by the receiver Pt robot. The frequency of sent signals was identical to the received signals. (**F**) Two Pt robots were able to communicate remotely across 1.2-m distance.

connector and Pt bellows tubes was achieved by short copper wires, and the silver paste was applied to ensure satisfactory electrical contact.

To complete the fabrication of dual-bellows Pt robot, we also connected two Pt tubes with air pumps and further sealed them with thin elastomer. The return loss (also known as $-S_{11}$) and the resonant frequency (RF) of the dipole antenna (i.e., the dual-bellows Pt robot) were measured at various compressive strains (from 0 to 50%) by a vector network analyzer. As shown in fig. S22, two resonant frequencies were observed at 218.3 and 741.8 MHz under 0% strain, and we selected the frequency with higher return loss at 741.8 MHz to investigate the strain responses of reconfigurable dipole antenna. As shown in Fig. 5C, the RF of dual-bellows Pt robot was strain dependent; the resonant frequencies increased from 741.8 to 783.5 MHz when the compressive strain increased from 0 to 50% (the length of dual-bellows Pt robot decreased). The increased RF was also confirmed by our simulation results (fig. S23). In addition, the electrical resistance of Pt-elastomer backbone increased under large compressive strains, which resulted in reduced return loss of dual-bellows robot. This strain-frequency relation kept stable even after 500 cycles of robotic actuations, which could be used as a robust indicator for remotely transmitting the actuating status of dual-bellows Pt robots. We further demonstrated the wireless communication between two Pt robots, which served as sender and receiver (Fig. 5D). Figure 5 (E and F) showed that the pulse signals at different frequencies (sent by the sender robot) could be well received by the receiver robot that was 1.2 m away, and no frequency deviation between the sent and received signals was observed. More discussion is provided regarding the effect of carbon on the strain sensing and wireless communication capabilities of Pt robots in the Supplementary Materials (figs. S24 and S25).

To show the technological advantages of GO-enabled metallic backbones, we further compared the Pt-elastomer backbones with several possible backbone materials, including cellulose papers, AFs, copper films on PDMS, multiwalled carbon nanotube (MWNT)–infiltrated papers, and poly(3,4-ethylenedioxythiophene)-poly(styrenesulfonate) (PDOT-PSS)–infiltrated papers (see detailed preparations in Materials and Method). The corresponding bellows-type robots fabricated with the above-mentioned materials were abbreviated as paper, AF, MWNT, and PDOT robots, respectively. Five categories of robotic features were compared, and their pros and cons are summarized in table S1 and discussed as follows.

1) Backbone density. The reported metallic backbone (i.e., Pt-PDMS, 0.4 g cm^{-3}) was lighter than commercial AF (2.7 g cm^{-3}), copper films on PDMS (1.1 g cm^{-3}), cellulose papers (1.2 g cm^{-3}), MWNT-infiltrated papers (1.3 g cm^{-3}), and PDOT-PSS–infiltrated papers (1.4 g cm^{-3}).

2) Mechanical stiffness. As shown in fig. S13, the Young's modulus of Pt-elastomer backbone was estimated to be 10 MPa, which was much lower than cellulose papers (580 MPa), MWNT-infiltrated papers (210 MPa), PDOT-PSS–infiltrated papers (230 MPa), copper film–coated silicon (300 MPa), and commercial AF (~70 GPa). High-stiffness materials (e.g., AF) caused difficulty in fabricating the origami robots with complex folding patterns (e.g., auxetic hexagonal origami).

3) Energy efficiency. With the lightweight and mechanically compliant Pt-elastomer backbones, the resulting dual-bellows Pt robot demonstrated more power-efficient actuating behaviors than the dual-bellows paper and AF robots (at same size and origami folds) (fig. S19).

4) Strain sensing capabilities. We further compared the strain sensing capabilities of single-bellows Pt, AF, MWNT, and PDOT robots in fig. S26. The Pt robot demonstrated efficient strain sensing capabilities with a GF of 0.17, whereas the AF and MWNT robots did not exhibit any strain response even under 40% elongation

(GFs close to 0.00). The PDOT robot presented a weak strain sensing performance (GF, ~0.01). The poor strain sensing capabilities of AF, MWNT, and PDOT robots resulted from high structural integrity of their conducting layers under various bending. On the other hand, the conductive Pt microfibers in the high-curvature region became less interdigitated under bending, resulting in larger strain responses in resistance for the Pt-elastomer backbones (Fig. 3G).

5) Wireless communication capabilities. The wireless communication capabilities of dual-bellows robots with different backbone materials were also compared (fig. S27). The Pt robot demonstrated efficient wireless communication capabilities with a return loss of 11.6 dB at its RF, whereas the return loss of PDOT robot was nearly zero. The AF and MWNT robots presented much lower and comparable wireless communication capabilities with return losses of 3.8 and 12.9 dB at their resonant frequencies, respectively.

Overall, only the Pt-elastomer backbone was able to integrate all of the advantages together into the resulting Pt robots, including light weight, mechanical compliance, low energy consumption, high-performance strain sensing, and efficient wireless communications.

The multifunctionality of Pt robots with built-in capabilities of resistive heating, strain sensing, and wireless communication is demonstrated in Fig. 6. As shown in Fig. 6A and movie S2, the conductive Pt-elastomer backbones enabled the as-fabricated robots to control their body temperature on-demand under different applied voltages. In this demonstration, two single-bellows Pt robots were fabricated and connected to air pumps. To present efficient thermal management, we froze two Pt robots in ice cubes, limiting their robotic actuations even under large input pressure. Under the applied voltage of 20 V, the surface temperature of upper Pt robot increased rapidly from 0° to 80°C with the gradual melting of surrounding ice layer. Next, the strain sensing capability of Pt robots enabled the real-time monitoring of robotic motions. The fabrication of a dual-bellows Pt robot is schematically illustrated in Fig. 6B. After the fabrication, the dual-bellows Pt robot was pneumatically actuated along a projected pathway consisting of three segments: (i) moving straight, (ii) turning right, and (iii) turning left (movie S3). As the Pt robot first crawled straight, both bellows tubes were pneumatically inflated/deflated to the same extent. The equal strains resulted in ~40 and ~50% relative current changes measured from the left and the right bellows tubes, respectively. The difference in current changes of two Pt tubes could be due to nonuniform elastomer coating on the templated Pt networks. Afterward, when nonequivalent strains were applied to bellows tubes, the Pt robot started to turn left or right. When the Pt robot turned right, the current change of left bellows decreased from ~40 to ~18%, whereas the right bellows

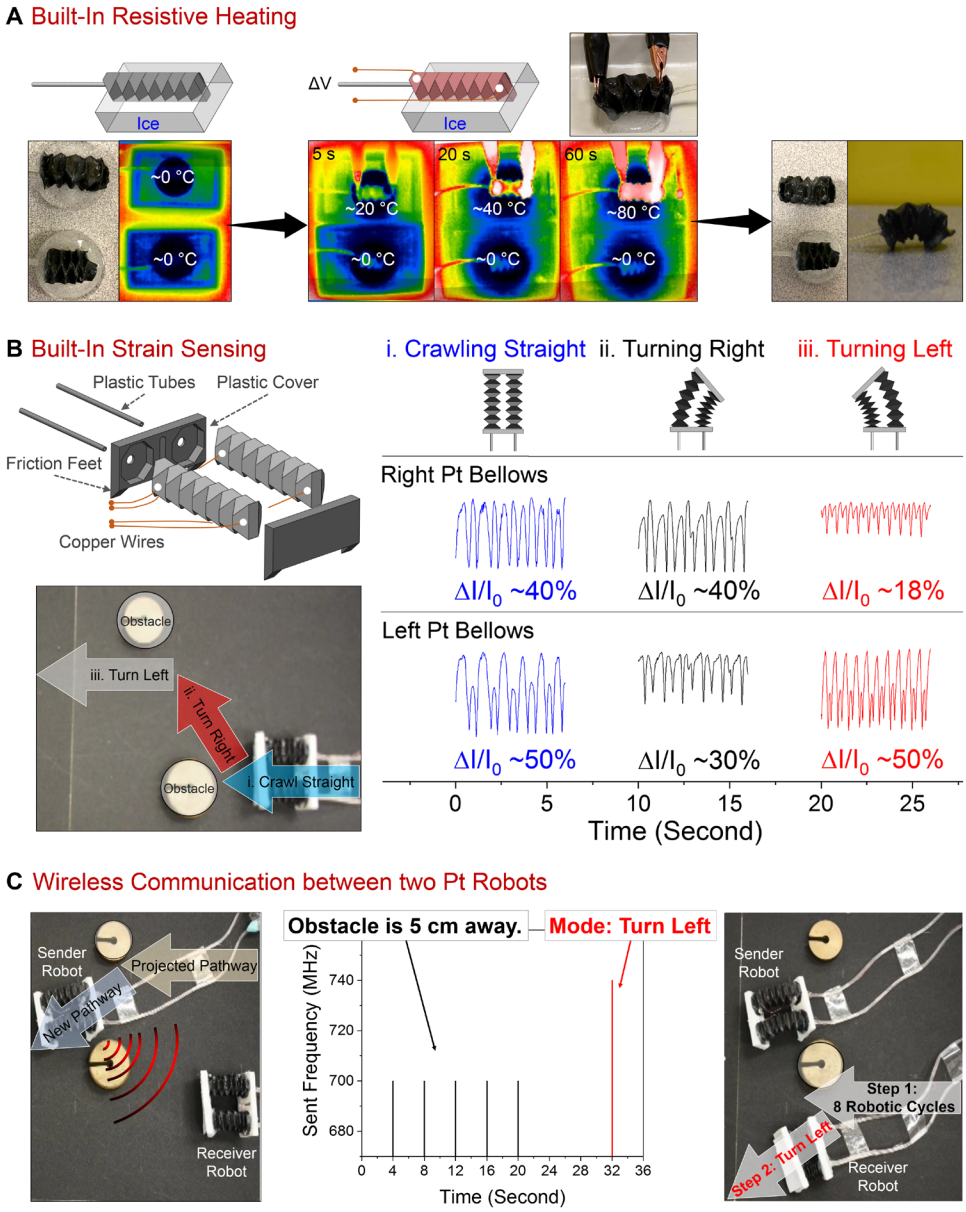

Fig. 6. Demonstrations of multifunctional Pt robots. (**A**) Single-bellows Pt robot with built-in resistive heating capability. Two Pt robots were frozen in ice cubes. Under an applied voltage of 20 V, the upper Pt robot was quickly heated to ca. 80°C in 60 s, escaped from the ice, and continued to crawl forward. (**B**) Dual-bellows Pt robot with built-in strain sensing capability. The Pt robotic backbones were connected with copper wires, and the connection was fixed using silver paste. The proposed pathway for the dual-bellows Pt robot involved (i) crawling straight, (ii) turning right, and (iii) turning left. The robotic actuations along the whole pathway were monitored by reading the current profiles of left and right Pt bellows tubes. (**C**) Wireless communication between two dual-bellows Pt robots. The sender robot was blocked by an obstacle on the projected pathway and turned left to bypass the obstacle. The sender robot sent a series of signals to the receiver robot. The signals were then interpreted into the moving guideline for the receiver robot, enabling the robot to take the proposed pathway without encountering the obstacle.

stayed at ~50%. When the robot turned left, the left bellows remained at ~40%, and the current change of right bellows went down to ~30%. In addition, the frequency of current fluctuations corresponded to the frequency of robotic actuations, enabling the users to monitor the robotic motions and experienced pathways by reading the current profiles of both Pt bellows tubes.

Furthermore, we demonstrated the wireless communication between two Pt robots with built-in antennas. As shown in Fig. 6C and movie S4 (the detailed setup was described in Materials and Methods), the sender robot was actuated along the projected pathway and encountered an obstacle halfway. Then, the sender robot was controlled to turn left to bypass the obstacle and sent the specific signals encoded with new pathway information. For instance, the sender robot sent out five pulses at 700 MHz with the gap of 4 s, followed by a strong pulse at 740 MHz, which can be interpreted as the moving guideline for the receiver robot to move straight for 5 cm and turn left afterward. The receiver robot well received the signals that were further translated into the corresponding orders of robotic actuations, involving two steps: (i) moving straight for eight inflation/deflation cycles and (ii) turning left by only actuating the left bellows tube. The receiver robot was able to bypass the obstacle by following the guided pathway.

To expand the applications of metallic robotic backbones and further address the challenges of limited scalability, we developed a Pt-GO-cellulose ink combined with fused deposition modeling (FDM) 3D printing to obtain the metallic robotic backbones with molded shapes (Fig. 7A). Generally, the paper origami templates were manually folded, which limited the production of robotic backbones with highly complex shapes and the potential in large-scale manufacturing. Instead of folding cellulose papers into origami templates, we prepared cellulose paper pulp by the assistance of ball milling followed by ultrasonication, and the pulp was then mixed with GO dispersion and $PtCl_4$ to obtain the Pt-GO-cellulose ink (see Materials and Methods for detailed preparation). The weight percentages of cellulose, GO, and Pt salt were controlled to 78.9, 15.0, and 6.1 wt %, which were the same as the composition of manually folded Pt-GO-cellulose templates. The Pt-GO-cellulose ink was then poured into an FDM 3D-printed mold followed by overnight air drying, and the Pt-GO-cellulose template was unmolded. By following similar two-stage annealing/calcination, the as-produced Pt replica showed a similar macroscale shape (with 51% dimension shrinkage) and fibrous microstructures, as shown in the SEM image in Fig. 7A.

Last, to further realize the concept of untethered Pt robots that can be remotely controlled via magnetic fields, we synthesized a tetrapod-shaped Pt replica using the Pt-GO-cellulose ink. The Pt replica was next infiltrated with the PDMS solution containing magnetic Nd–Fe–B particles (diameter, ~5 μm in fig. S28; raw material of neodymium magnet) to fabricate the Pt–(Nd–Fe–B) robotic backbones (see Materials and Methods for detailed preparations). Similar to the earlier findings, the Pt–(Nd–Fe–B) backbones fabricated via Pt-GO-cellulose ink also demonstrated built-in strain sensing and wireless communication capabilities, as shown in Fig. 7B. The multifunctional Pt–(Nd–Fe–B) tetrapods (Fig. 7B) were further put into strong magnetic field (more than 1 T; see Materials and Methods for setup), which induced the magnetic orientations to the tetrapods (Fig. 7C). Afterward, the Pt–(Nd–Fe–B) tetrapods were able to undergo reversible shape/body transformation under magnetic actuations (Fig. 7C) and became untethered to move forward by following the trajectories of rotating magnetic fields (Fig. 7D). We expected that this newly developed fabrication may provide alternative strategies to synthesize multifunctional robotic backbones and address the challenges of fabrication scalability. With the assistance of FDM 3D printing and the incorporation of magnetic particles, the Pt–(Nd–Fe–B) backbones may be further applied to various robotic designs and dimensions of soft robots and facilitate the development of magnetically actuated soft robots with built-in multifunctionality.

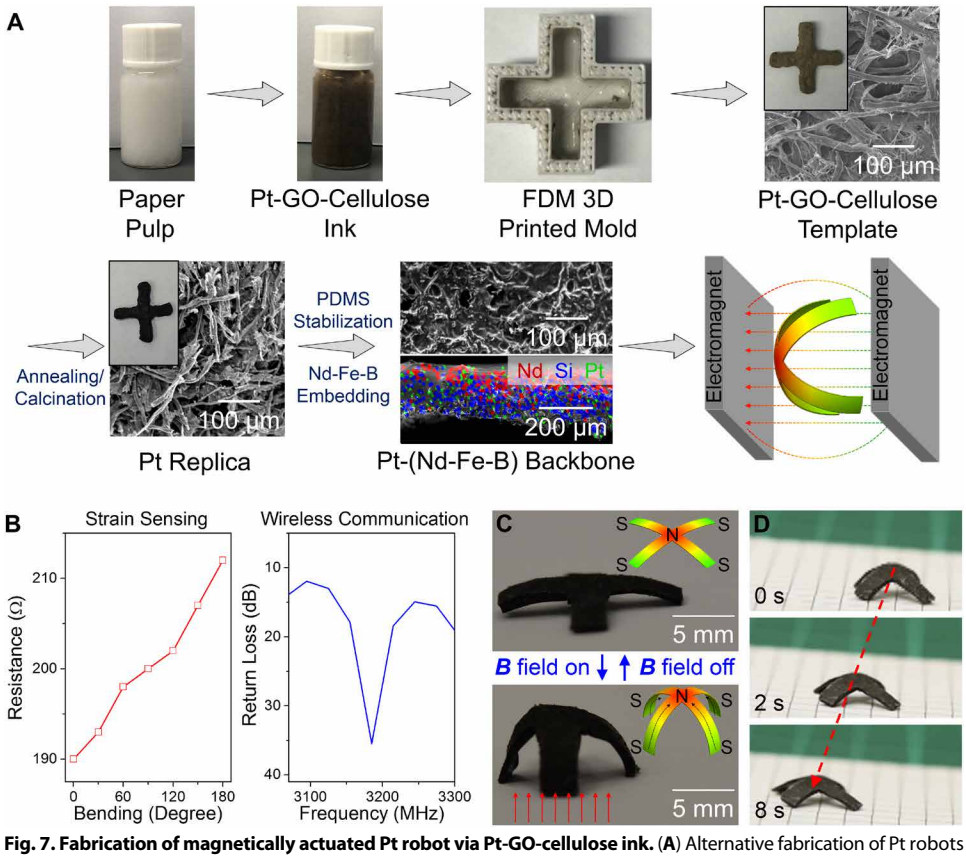

Fig. 7. Fabrication of magnetically actuated Pt robot via Pt-GO-cellulose ink. (**A**) Alternative fabrication of Pt robots was demonstrated by developing Pt-GO-cellulose ink and incorporating with FDM 3D printing. After two-stage annealing/calcination, PDMS stabilization, and embedding with Nd–Fe–B particles, a magnetically actuated Pt–(Nd–Fe–B) tetrapod robot was fabricated. (**B**) Built-in strain sensing and wireless communication capabilities of Pt–(Nd–Fe–B) tetrapod robot. (**C**) Pt–(Nd–Fe–B) tetrapod robot arched up and down under magnetic actuations. (**D**) Pt–(Nd–Fe–B) tetrapod robot moved forward by following the trajectories of rotating magnetic fields.

CONCLUSION

Here, we developed a GO-enabled templating synthesis to produce reconfigurable, compliant, multifunctional metallic backbones for the fabrication of origami robots with built-in strain sensing and wireless communication capabilities. The GO-enabled templating synthesis realized the production of complex noble metal origamis (including Ag, Au, and Pt) with high structural replication of their paper templates. The reproduced Pt origami structures were further stabilized with thin elastomer, and the Pt-elastomer origamis were reconfigurable and served as the multifunctional backbones for building origami robots. Compared with traditional papers, plastics, functional papers, and metal sheets, the reconfigurable Pt-elastomer backbones were more lightweight, deformable, and power efficient. The metallic backbones showed high adaptability to multiple actuation systems, including pneumatics, shape SMA, and magnet fields. In addition, the Pt robots demonstrated distinct capabilities without needing external electronics, such as on-demand resistive heating, strain sensing, and built-in wireless communication. The multifunctionality of Pt robots was further demonstrated—such as melting an ice cube to escape, monitoring/recording robotic motions in real time, and wireless communications for robot-robot interactions—extending the capabilities of traditional paper-based origami robots.

The metallic robotic backbones show high adaptability to multiple conventional actuation systems (such as pneumatics, SMA, and magnetic fields). These highly adaptable robotic backbones may be applied to various robotic designs developed in many other actuation systems, allowing other origami robots to have similar augmented functions (e.g., fire retardancy, strain sensing, and wireless communication) and maintaining their light weight and location-independent compliance. We expect that the metal-based origami robots are advantageous for a wide range of applications, such as robots that can work in high-risk environments (e.g., chemical spills and fire disaster), artificial muscles, humanoid robotic arms, and remote control of untethered robots. In addition, the metallic backbones may be further functionalized with electrochemically active materials, providing the opportunities to fabricate the energy storage devices on the robotic backbone. The development of such multifunctional metallic backbones enriches the material library for the fabrication of soft robotics toward high functional integration.

MATERIALS AND METHODS

Materials

Silver nitrate ($AgNO_3$), gold chloride ($AuCl_3$), platinum chloride ($PtCl_4$), and PDOT-PSS solutions were purchased from Sigma-Aldrich. MWNT dispersion was purchased from OCSiAl Ltd. The chromatography cellulose paper (size, 46 cm by 57 cm by 200 μm) was purchased from Thermo Fisher Scientific. GO (5 mg ml^{-1}, dispersion in water) was purchased from Angstron Materials. Nd–Fe–B particle was purchased from Magnequench International. Dichloromethane (99.9%) was purchased from J. T. Baker. PDMS (Sylgard 184) base and curing agent were purchased from Dow Corning Corporation. All reagents were used as received without further purification.

Preparation of M-GO-cellulose templates

The cut, folded papers were soaked into diluted GO dispersion (5 mg ml^{-1}) for 12 hours and air-dried to achieve the GO-cellulose composite templates. The GO-cellulose templates were then soaked in various metal salt solutions (0.1 M) for another 12 hours and air-dried to obtain the M-GO-cellulose.

Two-stage annealing/calcination processes for creation of metal replicas

The M-GO-cellulose origami was put into a tube furnace (Thermal Craft, Polaris Science Pte. Ltd.) and annealed under argon with a specific heating program: set temperature, 800°C; ramp time, 1 hour; and hold time, 2 hours. After the furnace cooled, the origami replica was calcined under air for another 1 hour at various temperatures from 200° to 600°C. After the furnace was cooled down naturally, the as-synthesized metal replicas were taken out carefully.

Fabrication of metal-elastomer composites

The PDMS solution was prepared by mixing PDMS curing agent and base in a 1-to-10 weight ratio and diluting with dichloromethane (from 100 to 500 mg ml^{-1}). The PDMS solution was slowly infiltrated into the structures of noble metal replicas, followed by the curing process in an oven at 70°C for 3 hours. The optimized concentration of dilute PDMS solution was found to be 300 mg ml^{-1}.

Uniaxial tension testing

The cellulose paper (~250 μm thick), templated Pt film (~50 μm thick), Pt-PDMS film (~90 μm thick), and Pt-PDMS honeycomb metamaterials (~90 μm thick) were secured onto a tensile tester (Instron 5543, Instron, USA) with a 500-N load cell. The load cell was calibrated before the testing. The sample was pulled with an extension rate of 5 mm min^{-1} until the paper- or Pt-based sample was broken. A fatigue test was performed on the Pt-PDMS honeycomb metamaterials for 200 cycles with 55% uniaxial strain.

Fabrication of SMA-actuated Pt actuator

The SMA wires (150-μm-diameter nitinol wire; FLEXINOL, DYNALLOY Inc.) were shaped with a 3D-printed mold at 300°C. Afterward, the nitinol wires were bent into a "U" shape and glued onto the surface of Pt-elastomer auxetic hexagonal origami. The SMA wires at the martensite state were compliant and conformed to the curvature of Pt-elastomer origami. When we applied current (1.7 A) to heat up the nitinol wires, the U-shaped wires reverted to the austenite state and straightened out, causing the Pt-elastomer origami to bend. When current was cut, the wires were cooled and reverted to the martensite state, allowing the Pt-elastomer origami to recover.

Fabrication of pneumatic single-bellows Pt robot

A Pt-GO-cellulose bellows origami was assembled with two planar Pt-GO-cellulose templates with the Pt-GO glue (fig. S30). The preparation of Pt-GO glue was similar to the reported protocol in the literature (*25*). Briefly, the metalized GO glue was prepared by mixing polyvinyl alcohol (PVA) (200 mg ml^{-1}), GO dispersion (1 mg ml^{-1}), and metal salt ($PtCl_4$, 0.2 M) in water, followed by the ultrasonication (SONICA 5200) for 5 hours. After connecting with Pt-GO glue, the origami assembly template underwent two-stage annealing/calcination processes to produce an enclosed Pt bellows tube replica. The Pt replica was then stabilized with a thin layer of PDMS, and a pneumatic channel was connected to the Pt-PDMS bellows tube. The connection was further sealed with a thin layer of PDMS to ensure that there were no air gaps/pores. The pneumatic single-bellows Pt robot was actuated by an air pump, and the actuating behaviors were recorded by a camera. The directional friction of bellows-type Pt robots came

from the friction feet installed at the head and tail of the Pt robot. For the single-bellows robot, the friction feet were made with silicon.

Fabrication of pneumatic dual-bellows Pt robot

Two enclosed Pt-PDMS bellows tubes were prepared from Pt-GO-cellulose bellows origamis, and two Pt replicas were further stabilized with PDMS. The pneumatic channels and plastic covers were connected to two Pt-PDMS bellows tubes to finish the robotic assembly (fig. S16). In the end, the connections were further sealed with PDMS to ensure that there were no air gaps/pores, and the pneumatic dual-bellows Pt robot was actuated by air pumps. The directional friction of bellows-type Pt robots came from the friction feet installed at the head and tail of Pt robot. For the dual-bellows robot, 3D-printed plastic feet were adopted.

Fabrication of pneumatic bellows-type robots by cellulose papers, MWNT-infiltrated papers, PDOT-PSS–infiltrated papers, and AFs

Single-bellows and dual-bellows robots were assembled by following the procedures in figs. S16 and S30. Bellows tubes were manually folded using cellulose papers, and then, the paper bellows tubes were soaked in MWNT dispersion (~8 mg ml^{-1} in *N*-methyl-2-pyrrolidone) and PDOT-PSS solution (1.1 wt % in water). After a vacuum drying process, we sealed the MWNT-infiltrated and PDOT-PSS–infiltrated origamis by thin elastomer and connected them to air pumps for the fabrication of pneumatic bellows-type robots (MWNT robot and PDOT robot). On the other hand, we manually folded AFs into bellows origamis and then sealed them by thin elastomer and connected them to air pumps for the fabrication of pneumatic robots (AF robot).

Calculation of energy consumption of dual-bellows robots

The dual-bellows robots with different backbone materials were actuated by syringe pumps. During the robotic actuations, the gas pressure and syringe displacements were recorded, and the energy consumption (E) was calculated using the following equation

$$E = \int P \cdot A \cdot S dt$$

where P refers to the gas pressure, A denotes the cross-sectional area of syringe pumps, and S represents syringe displacements.

Setup for resistive heating of Pt-PDMS origamis and Pt robots

The Pt-PDMS origamis and bellows-type Pt robots were glued with copper wires and connected to a Keithley 2400 SourceMeter to apply voltage. The surface temperatures of Pt-PDMS origamis and Pt robots were measured by a thermocouple (TC-08, Pico Technology, UK), and the temperature distribution was measured using an infrared camera (HT-02, XINTEST, China).

Numerical simulation of reconfigurable dipole Pt antenna

We simulated the far-field radiation pattern of reconfigurable dipole Pt antenna in terms of electric field intensity as a function of space coordinate $E(x, y, z)$. The radiation pattern graphically represents the spatial distribution of the strength of EM wave radiated from the dipole antenna. The radiation pattern contains the information and evaluations of an antenna, such as radiation intensity and directivity. The electric field as a function of space $E(x, y, z)$ of an ideal dipole antenna can be expressed by solving the Maxwell equations. We solved the Maxwell equations in a simulation software (Computer Simulation Technology) by finite element method in the frequency domain. The boundary conditions are open boundaries in all directions during the simulation. The size of bellows structures was set to be 5 cm. The electrical conductivity of Pt-elastomer bellows backbone was measured and set to be 485 S m^{-1}, and the relative permittivity and relative permeability were set to be 2.76 and 1.00, respectively. The waveguide ports were used to calculate the radiation patterns. The radiation pattern graphically represents the spatial distribution of the strength of EM wave radiated from the dipole antenna.

The radiation pattern contains the information, such as radiation intensity and directivity, which are the important evaluations of an antenna. The transmitted power was calculated using the following equations

$$\text{Return loss} = -10\log_{10}\frac{P_r}{P_i}$$

$$P_t = 1 - P_r$$

where P_r and P_i ($P_i = 1$ in this case) are the reflected and incident powers, respectively, and P_t is the transmitted power. Therefore, on the basis of the value of return loss, P_r and P_t could be calculated by the above equations.

Measurement of built-in strain sensors and reconfigurable dipole Pt antenna

Two pneumatic dual-bellows Pt robots were fabricated following the above-mentioned procedures, and two Pt robots were actuated by syringe pumps. To measure the performance of built-in strain sensing, we glued four copper wires on the surface of dual-bellows Pt robot by silver paint (Ted Pella Inc.) and connected them to AutoLab (Metrohm Singapore Pte. Ltd.) (Fig. 6B). When non-equivalent strains were applied to two bellows tubes, the Pt robot started to turn left or right. During the robotic actuations, AutoLab recorded the resistance changes of two bellows tubes of each Pt robot in real time.

For wireless communication, the dual-bellows Pt robot was connected to the RF instruments by RF coaxial cables and SubMiniature version A connectors. The return loss of Pt robot was measured by a vector network analyzer (N9915A FieldFox, Keysight Technologies). To enable the wireless communication between Pt robots, we fabricated two dual-bellows robots: One Pt robot (as the sender) was connected to an RF signal generator (Model 835, Berkeley Nucleonics) to send the signals at different frequencies (from 700 to 780 MHz) with the power of 0 dBm, and the other Pt robot (as the receiver) was connected to an RF spectrum analyzer (N9000B; Keysight Technologies) to receive and analyze signals.

Preparation of cellulose paper pulp and Pt-GO-cellulose ink

The cellulose paper was first cut into small pieces (2 mm by 2 mm) and mixed with water (10 wt % of paper). The mixture was stirred under 100°C for 24 hours, followed by ball milling (500 rpm) for 6 days and continuous tip sonication for 3 days to obtain well-dispersed paper pulp. GO dispersion and $PtCl_4$ were then added into the prepared paper pulp to achieve the Pt-GO-cellulose ink; the concentrations of GO and Pt ions were kept at 0.75 mg ml^{-1} and 0.018 M, respectively, to produce the Pt-GO-cellulose templates with the same weight percentages of manually folded Pt-GO-cellulose templates (cellulose, 78.9 wt %; GO, 15.0 wt %; and Pt salt, 6.1 wt %).

Fabrication of magnetically responsive Pt–(Nd–Fe–B) tetrapod robot

The Pt-GO-cellulose ink was poured into an FDM 3D-printed mold followed by overnight air drying, and the Pt-GO-cellulose template with tetrapod shape was molded (Fig. 7A). By following similar two-stage annealing/calcination, we obtained the Pt replica with tetrapod shape. Then, the PDMS solution was prepared by mixing PDMS curing agent and base in a 1-to-10 weight ratio and diluting with dichloromethane (300 mg ml^{-1}), and Nd–Fe–B particles were added to the PDMS solution (100 mg ml^{-1}), followed by ultrasonication for 1 hour. The dilute PDMS solution containing Nd–Fe–B particles was slowly infiltrated into the structures of Pt tetrapods, followed by the curing process at 70°C for 3 hours.

Setup for the actuations of Pt–(Nd–Fe–B) tetrapod robot

The Pt–(Nd–Fe–B) tetrapods was first molded (as shown in Fig. 7A) and put into the space between two electromagnets with high field uniformity (at 1.2 T; EM4-HVA-S, Lake Shore Cryotronics), which induced the magnetic orientations to the tetrapods (Fig. 7C). Afterward, the Pt–(Nd–Fe–B) tetrapods were able to undergo reversible shape/body transformation under magnetic actuations (0.5 turns/s) (Fig. 7C) and became untethered to move forward at a speed of 1.1 mm s^{-1} by following the trajectories of rotating magnetic fields (movie S5).

Characterization and measurements

XRD patterns were measured using an x-ray diffractometer [D8 ADVANCE x-ray powder diffractometer, Bruker; Cu Kα ($\lambda = 0.154$ nm) radiation] at a scan rate of 4° min^{-1}. The morphologies of cellulose paper and templated metallic structures were characterized using an SEM (FEI Quanta 600) and a high-resolution TEM (JEOL 2010F). The sample area, characteristic diameter, and porosity were quantified by the measurements of grayscale line profiles of the micrographs and photos using ImageJ. The resistance of metal replicas was measured using Industrial MultiMeter (EX503), and the real-time resistance changes of Pt-elastomer origamis were monitored using AutoLab (Metrohm Singapore Pte. Ltd.).

SUPPLEMENTARY MATERIALS

robotics.sciencemag.org/cgi/content/full/4/33/eaax7020/DC1

Fig. S1. XRD spectra of GO after metal ion intercalation and after first-stage annealing.
Fig. S2. Photos and SEM images of cellulose paper, GO-cellulose template, C/metal intermediate products, and metal replicas.
Fig. S3. SEM images and EDS analysis of Ag products after the calcination in air at different temperatures.
Fig. S4. SEM images and EDS analysis of Au products after the calcination in air at different temperatures.
Fig. S5. SEM images and EDS analysis of Pt products after the calcination in air at different temperatures.
Fig. S6. Raman spectra of Pt replicas after the calcination in air at different temperatures.
Fig. S7. Cross-sectional SEM images of Ag, Au, and Pt products after the calcination in air at different temperatures.
Fig. S8. Thickness, dimension shrinkage, and mechanical properties of noble metal replicas.
Fig. S9. Weight changes of Pt-GO-cellulose and Pt-cellulose origamis at different annealing/calcination stages.
Fig. S10. EDS mapping analysis of Pt products from GO-cellulose and cellulose-only templates.
Fig. S11. TEM image of annealed Pt nanocrystals from Pt-GO-cellulose template.
Fig. S12. Engineering thickness and electrical conductivity of Pt-elastomer backbones.
Fig. S13. Stress-strain curves of cellulose papers, PDOT-PSS–infiltrated papers, MWNT-infiltrated papers, copper film on silicon, planar Pt replica, and Pt-PDMS films.
Fig. S14. Relative resistance changes of a flat Pt-PDMS film under repetitive 90° bending.
Fig. S15. Photos of the bellows tubes of paper predecessor and the elastomer-stabilized Pt replica.
Fig. S16. Design of single-bellows Pt robot with friction feet.
Fig. S17. SEM image of commercial cellulose paper.
Fig. S18. Digital photo of pneumatic single-bellows paper and Pt robots.
Fig. S19. Performances of Pt robot, paper robot, and AF robot.
Fig. S20. Fabrication process of pneumatic dual-bellows Pt robot.
Fig. S21. Design of dual-bellows Pt robot with friction feet.
Fig. S22. Return loss of dual-bellows Pt robot with a broad bandwidth from 0 to 1200 MHz.
Fig. S23. Simulation results of reconfigurable dipole Pt antenna (i.e., dual-bellows Pt robot).
Fig. S24. Strain sensing of flat Pt-PDMS composites with different amounts of carbon.
Fig. S25. Return loss of dipole antennas made from flat Pt-PDMS films with different amounts of carbon.
Fig. S26. Relative resistance changes under various uniaxial strains of various dual-bellows robots, including Pt robot, AF robot, MWNT robot, and PDOT robot.
Fig. S27. Return loss of different reconfigurable dipole antennas (i.e., dual-bellows robots), including Pt robot, PDOT robot, MWNT robot, and AF robot.
Fig. S28. SEM image of Nd-Fe-B particles.
Fig. S29. Return loss of hexagonal honeycomb Pt-elastomer origami.
Fig. S30. Assembly of an enclosed bellows Pt tube.
Table S1. Comparison among various possible backbone materials.
Movie S1. Comparison of gas pressure between paper and Pt robots.
Movie S2. Origami Pt robot with built-in resistive heating.
Movie S3. Origami Pt robot with built-in strain sensing.
Movie S4. Wireless communication of origami Pt robots.
Movie S5. Magnetically actuated Pt-(Nd-Fe-B) tetrapod robot.

REFERENCES AND NOTES

1. J. L. Silverberg, A. A. Evans, L. McLeod, R. C. Hayward, T. Hull, C. D. Santangelo, I. Cohen, Using origami design principles to fold reprogrammable mechanical metamaterials. *Science* **345**, 647–650 (2014).
2. D. Rus, M. T. Tolley, Design, fabrication and control of origami robots. *Nat. Rev. Mater.* **3**, 101–112 (2018).
3. Q. Zhang, Q. Jiang, N. Li, L. Dai, Q. Liu, L. Song, J. Wang, Y. Li, J. Tian, B. Ding, DNA origami as an in vivo drug delivery vehicle for cancer therapy. *ACS Nano* **8**, 6633–6643 (2014).
4. Q. Jiang, C. Song, J. Nangreave, X. Liu, L. Lin, D. Qiu, Z.-G. Wang, G. Zou, X. Liang, H. Yan, B. Ding, DNA origami as a carrier for circumvention of drug resistance. *J. Am. Chem. Soc.* **134**, 13396–13403 (2012).
5. J. Morgan, S. P. Magleby, L. L. Howell, An approach to designing origami-adapted aerospace mechanisms. *J. Mech. Des.* **138**, 052301 (2016).
6. P. Badagavi, V. Pai, A. Chinta, Use of origami in space science and various other fields of science, in *2017 2nd IEEE International Conference on Recent Trends in Electronics, Information & Communication Technology (RTEICT)* (IEEE, 2017), pp. 628–632.
7. Z. Song, T. Ma, R. Tang, Q. Cheng, X. Wang, D. Krishnaraju, R. Panat, C. K. Chan, H. Yu, H. Jiang, Origami lithium-ion batteries. *Nat. Commun.* **5**, 3140 (2014).
8. M. Nogi, N. Komoda, K. Otsuka, K. Suganuma, Foldable nanopaper antennas for origami electronics. *Nanoscale* **5**, 4395–4399 (2013).
9. S. Li, D. M. Vogt, D. Rus, R. Wood, Fluid-driven origami-inspired artificial muscles. *Proc. Natl. Acad. Sci. U.S.A.* **114**, 13122–13137 (2017).
10. S. Felton, M. Tolley, E. Demaine, D. Rus, R. Wood, A method for building self-folding machines. *Science* **345**, 644–646 (2014).
11. J. A. Faber, A. F. Arrieta, A. R. Studart, Bioinspired spring origami. *Science* **359**, 1386–1391 (2018).
12. S. Miyashita, S. Guitron, S. Li, D. Rus, Robotic metamorphosis by origami exoskeletons. *Sci. Robot.* **2**, eaao4369 (2017).
13. T. J. Wallin, J. Pikul, R. F. Shepherd, 3D printing of soft robotic systems. *Nat. Rev. Mater.* **3**, 84–100 (2018).
14. X. Zang, C. Shen, Y. Chu, B. Li, M. Wei, J. Zhong, M. Sanghadasa, L. Lin, Laser-induced molybdenum carbide–graphene composites for 3D foldable paper electronics. *Adv. Mater.* **30**, 1800062 (2018).
15. Y. Kim, H. Yuk, R. Zhao, S. A. Chester, X. Zhao, Printing ferromagnetic domains for untethered fast-transforming soft materials. *Nature* **558**, 274–279 (2018).
16. B. Mosadegh, P. Polygerinos, C. Keplinger, S. Wennstedt, R. F. Shepherd, U. Gupta, J. Shim, K. Bertoldi, C. J. Walsh, G. M. Whitesides, Pneumatic networks for soft robotics that actuate rapidly. *Adv. Funct. Mater.* **24**, 2163–2170 (2014).
17. F. Qiu, L. Zhang, S. Tottori, K. Marquardt, K. Krawczyk, A. Franco-Obregón, B. J. Nelson, Bio-inspired microrobots. *Mater. Today* **15**, 463 (2012).
18. M. A. McEvoy, N. Correll, Materials that couple sensing, actuation, computation, and communication. *Science* **347**, 1261689 (2015).
19. G.-Z. Yang, J. Bellingham, P. E. Dupont, P. Fischer, L. Floridi, R. Full, N. Jacobstein, V. Kumar, M. McNutt, R. Merrifield, B. J. Nelson, B. Scassellati, M. Taddeo, R. Taylor, M. Veloso, Z. L. Wang, R. Wood, The grand challenges of *Science Robotics*. *Sci. Robot.* **3**, eaar7650 (2018).

20. D. C. Christodouleas, F. C. Simeone, A. Tayi, S. Targ, J. C. Weaver, K. Jayaram, M. T. Fernández-Abedul, G. M. Whitesides, Fabrication of paper-templated structures of noble metals. *Adv. Mater. Technol.* **2**, 1600229 (2017).
21. M. Islam, J. Flach, R. Martinez-Duarte, Carbon origami: A method to fabricate lightweight carbon cellular materials. *Carbon* **133**, 140–149 (2018).
22. P.-Y. Chen, M. Liu, Z. Wang, R. H. Hurt, I. Y. Wong, From flatland to spaceland: Higher dimensional patterning of two-dimensional materials. *Adv. Mater.* **29**, 1605096 (2017).
23. P.-Y. Chen, M. Liu, T. M. Valentin, Z. Wang, R. Spitz Steinberg, J. Sodhi, I. Y. Wong, R. H. Hurt, Hierarchical metal oxide topographies replicated from highly textured graphene oxide by intercalation templating. *ACS Nano* **10**, 10869–10879 (2016).
24. M. Liu, P.-Y. Chen, R. H. Hurt, Graphene inks as versatile templates for printing tiled metal oxide crystalline films. *Adv. Mater.* **30**, 1705080 (2018).
25. H. Yang, B. S. Yeow, T.-H. Chang, K. Li, F. Fu, H. Ren, P.-Y. Chen, Graphene oxide-enabled synthesis of metal oxide origami for soft robotics. *ACS Nano* **13**, 5410–5420 (2019).
26. D. Li, M. B. Müller, S. Gilje, R. B. Kaner, G. G. Wallace, Processable aqueous dispersions of graphene nanosheets. *Nat. Nanotechnol.* **3**, 101–105 (2008).
27. S.-M. Bak, R. Qiao, W. Yang, S. Lee, X. Yu, B. Anasori, H. Lee, Y. Gogotsi, X.-Q. Yang, Na-ion intercalation and charge storage mechanism in 2D vanadium carbide. *Adv. Energy Mater.* **7**, 1700959 (2017).
28. E.-Y. Choi, T. H. Han, J. Hong, J. E. Kim, S. H. Lee, H. W. Kim, S. O. Kim, Noncovalent functionalization of graphene with end-functional polymers. *J. Mater. Chem.* **20**, 1907–1912 (2010).
29. K. Otto, I. Oja Acik, M. Krunks, K. Tõnsuaadu, A. Mere, Thermal decomposition study of $HAuCl_4{\cdot}3H_2O$ and $AgNO_3$ as precursors for plasmonic metal nanoparticles. *J. Therm. Anal. Calorim.* **118**, 1065–1072 (2014).
30. S.-M. Yoon, U. J. Kim, A. Benayad, H. Lee, H. Son, H.-J. Shin, W. M. Choi, Y. H. Lee, Y. W. Jin, E.-H. Lee, S. Y. Lee, J.-Y. Choi, J. M. Kim, Thermal conversion of electronic and electrical properties of $AuCl_3$-doped single-walled carbon nanotubes. *ACS Nano* **5**, 1353–1359 (2011).
31. W. K. Jozwiak, T. P. Maniecki, Influence of atmosphere kind on temperature programmed decomposition of noble metal chlorides. *Thermochim. Acta* **435**, 151–161 (2005).
32. W. P. Hoffman, Activation of carbon fiber surfaces by means of catalytic oxidation. U.S. Patent Appl. 5271917 (1993).

Acknowledgments: We thank C. C. Yap, Y. T. Elden, and H.K. S/O Tamil Selvan from National University of Singapore (NUS) High School for sample preparation. **Funding:** Faculty Research Committee Start-Up Grant of NUS (R-279-000-515-133), Ministry of Education Academic Research Fund Tier 1 Funds (R-279-000-532-114, R-397-000-297-114, and R-279-000-551-114) and Tier 2 Fund (R-279-000-579-112), AME Young Investigator Research Grant (A*STAR grant nos. A1884c0017 and R-279-000-546-305), Singapore-MIT Alliance for Research and Technology Ignition Grant (R-279-000-572-592), and NMRC Bedside and Bench under grant R-397-000-245-511. **Author contributions:** P.-Y.C., H.Y., B.S.Y., and Z.L. designed experiments. H.Y. carried out the material synthesis and characterizations. H.Y. and T.-H.C. conducted tension tests. B.S.Y. and H.Y. designed origami robots, performed actuation demonstrations and analyses, and realized the strain sensing concept. H.Y. and Z.L. realized the wireless communication concept. P.-Y.C. and H.Y. cowrote the manuscript. T.-H.C., K.L., L.J., Y.L., J.S.H., and H.R. were involved in the discussion and manuscript modification. R.H., J.S.H., and P.-Y.C. supervised the project. **Competing interests:** The authors declare that they have no competing interests. **Data and materials availability:** All data needed to support the conclusions of this manuscript are included in the main text and the Supplementary Materials. Contact P.-Y.C. (checp@nus.edu.sg) and H.Y. (e0276478@u.nus.edu) for materials.

Submitted 16 April 2019
Accepted 6 August 2019
Published 28 August 2019
10.1126/scirobotics.aax7020

Citation: H. Yang, B. S. Yeow, Z. Li, K. Li, T.-H. Chang, L. Jing, Y. Li, J. S. Ho, H. Ren, P.-Y. Chen, Multifunctional metallic backbones for origami robotics with strain sensing and wireless communication capabilities. *Sci. Robot.* **4**, eaax7020 (2019).

Science Robotics

Multifunctional metallic backbones for origami robotics with strain sensing and wireless communication capabilities

Haitao Yang, Bok Seng Yeow, Zhipeng Li, Kerui Li, Ting-Hsiang Chang, Lin Jing, Yang Li, John S. Ho, Hongliang Ren, and Po-Yen Chen

Sci. Robot. **4** (33), eaax7020. DOI: 10.1126/scirobotics.aax7020

Science Robotics (ISSN 2470-9476) is published by the American Association for the Advancement of Science. 1200 New York Avenue NW, Washington, DC 20005. The title *Science Robotics* is a registered trademark of AAAS.